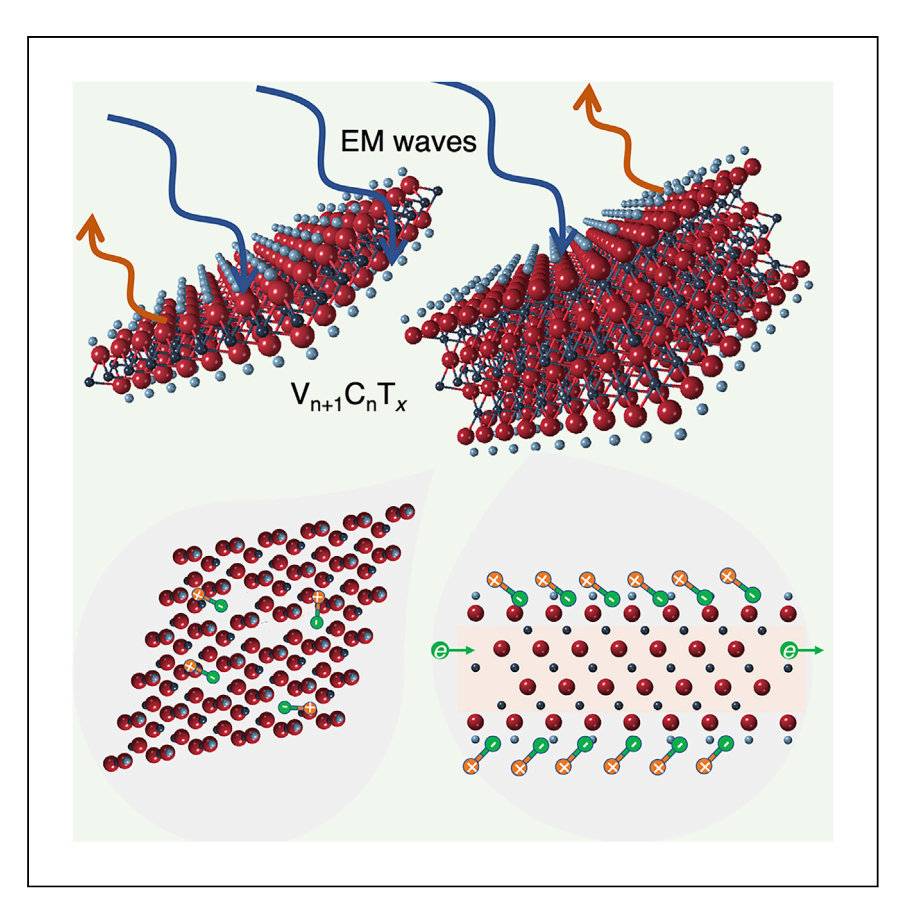


Article

Efficient microwave absorption with $V_{n+1}C_nT_x$ MXenes



Han et al. report that vanadium-based MXenes (V_2CT_x and $V_4C_3T_x$) can provide broadband microwave absorption with ultralow filler loading in polymer matrix. The free electron transport, surface terminations, native defects, and layers arrangement significantly affect electronic and dielectric properties of $V_{n+1}C_nT_x$ MXenes.

Meikang Han, Christopher E. Shuck, Akash Singh, ..., Vivek B. Shenoy, Eric A. Stach, Yury Gogotsi

gogotsi@drexel.edu

Highlights

Polyurethane composites with ~ 2 wt % $V_{n+1}C_nT_x$ absorb >90% of microwaves in X band

600-nm-thick $V_{n+1}C_nT_x$ films provide effective electromagnetic interference shielding

The native defects and surface groups affect the microwave absorption behavior

Han et al., Cell Reports Physical Science $\it 3$, 101073

October 19, 2022 © 2022 The Author(s). https://doi.org/10.1016/j.xcrp.2022.101073





Article

Efficient microwave absorption with $V_{n+1}C_nT_x$ MXenes

Meikang Han,^{1,2,4} Christopher E. Shuck,^{1,2} Akash Singh,³ Yizhou Yang,² Alexandre C. Foucher,³ Adam Goad,^{1,2} Bernard McBride,^{1,2} Steven J. May,² Vivek B. Shenoy,³ Eric A. Stach,³ and Yury Gogotsi^{1,2,5,*}

SUMMARY

The availability of MXenes and other two-dimensional conductive nanomaterials with tunable surface chemistry has reshaped the field of electromagnetic protection. However, the high electrical conductivity and low dielectric loss of titanium-based MXenes lead to strong reflection of electromagnetic waves, even when combined with polymers to form composites. Here, we report on the ability of vanadium-based MXenes to provide broadband microwave absorption. Polyurethane composites with ${\sim}2$ wt % $V_{n+1}C_{n}T_{x}$ can absorb 90% of electromagnetic waves covering the entire X band. In addition, pure $V_{n+1}C_nT_x$ films of submicrometer thickness can provide effective electromagnetic interference shielding. The free electron transport, surface terminations, native defects, and layers arrangement in composites have profound effects on electronic and dielectric properties of $V_{n+1}C_nT_x$ MXenes. This study points toward a new frontier for development of thin and highly absorbing MXene-based electromagnetic protection materials.

INTRODUCTION

With the increasing integration density and extension of operation frequencies of modern electronics, electromagnetic interference (EMI) shielding has become essential to protect electronic devices against destructive signal jamming. 1-3 Conventional EMI shielding is typically accomplished using metals that reflect most of the incident electromagnetic (EM) waves. However, these reflected waves cause secondary EM pollution, which can still harm device-to-device interactivities. Hence, an "ideal" EMI shielding material would absorb unwanted EM radiation rather than reflect it.

Since 2016, more than a dozen MXenes, which are two-dimensional (2D) transition-metal carbides and/or nitrides, have shown record-breaking EMI shielding capability in thin films/coatings, owing to their high metallic conductivity. A-B For example, a $\sim\!40$ nm-thick $Ti_3C_2T_x$ MXene coating offers an EMI shielding effectiveness (SE) of 21 dB, which exceeds the commercial shielding requirements. More recently, thermally annealed Ti_3CNT_x was demonstrated to have exceptional shielding performance with anomalously high EMI SE of absorption (SEA), despite having a lower electrical conductivity than $Ti_3C_2T_x$. While EMI shielding includes contributions from both reflection and absorption, the shielding behavior of all pure MXenes is still dominated by reflection rather than absorption. This behavior arises because high electrical conductivity (generally >100 S cm $^{-1}$) and efficient EM wave absorption is hindered by the impedance mismatch with free space. Microwave absorption

¹A.J. Drexel Nanomaterials Institute, Drexel University, Philadelphia, PA 19104, USA

²Department of Materials Science and Engineering, Drexel University, Philadelphia, PA 19104, USA

³Department of Materials Science and Engineering, University of Pennsylvania, Philadelphia, PA 19104, USA

⁴Present address: Institute of Optoelectronics, Fudan University, Shanghai 200438, China

⁵Lead contact

*Correspondence: gogotsi@drexel.edu https://doi.org/10.1016/j.xcrp.2022.101073





materials, which deplete the incident EM waves and transform microwave energy into heat, offer an alternative approach. ¹⁰ In the past 5 years, Ti₃C₂T_x-based composites with an EM wave-transparent matrix were designed to balance impedance match and EM wave attenuation. However, the pristine Ti₃C₂T_x/polymer composites show relatively high permittivity ($\varepsilon = \varepsilon' - j\varepsilon''$) and low dielectric loss in the gigahertz range, whereas both moderate permittivity (ε' , \sim 4–20 and ε'' , \sim 2–10) and high tangential loss (tan $\delta = \varepsilon''/\varepsilon'$; \sim 0.5) are necessary for ideal EM wave absorption materials. ^{10–12} For example, the tangential loss of 10 wt % Ti₃C₂T_x MXene/polyvinyl alcohol composite fabricated by vacuum-assisted filtration is only ~0.09. 11 This implies that Ti₃C₂T_x/polymer composites can hardly achieve efficient absorption in a broad frequency range. In order to broaden the absorption bandwidth for radar stealth and electronic applications, considerable research has focused on adding additional EM-absorbing components to Ti₃C₂T_x, by analogy with reduced graphene oxide. They include magnetic particles, carbon materials, and semiconductors with high dielectric loss (details are listed in Table S1) to achieve a synergistic effect between various EM dissipation behaviors (polarization loss, magnetic loss, conductor loss, etc.). 13,14 However, this weakens the merits of MXenes due to the increased filler loading and complicated interface design, in contrast to conventional ferrites and carbon-based absorption materials. Hence, it is still challenging to produce light-weight, broadband, and efficient MXene-based microwave absorbers. When considering their tunable surface chemistry, abundant free charge carriers, and anisotropic electron transport, MXenes still show a great potential for designing microwave absorbers. 15 Besides Ti₃C₂T_x, over 30 stoichiometric MXenes have been experimentally synthesized and multiple solid solutions reported. 16,17 However, little is known about their dielectric properties, which are critical for increasing EM absorption.

In this study, we report on fundamental dielectric responses, microwave absorption, and EMI shielding capability of $V_{n+1}C_nT_x$ (n = 1 or 3) MXenes. The electronic properties of V_2CT_x and $V_4C_3T_x$ were predicted and experimentally investigated to understand charge transport in those MXenes. ¹⁸ We demonstrate that $V_{n+1}C_nT_x$ MXenes with ultralow loading (\sim 2 wt %) in polyurethane (PU) matrix achieve effective microwave absorption (>90% of EM waves are absorbed) over the whole X band (8.2–12.4 GHz, the most common radar frequency range), which outperforms $Ti_3C_2T_x$ -based, carbon-based, and conventional ferrite-based EM wave absorption materials. The modest dielectric loss of vanadium-based MXenes, together with their 2D nature, adjustable surface chemistry, and high carrier transport, provide a more promising platform than $Ti_3C_2T_x$ for the design and optimization of microwave absorbers, which are of importance for defense (e.g., radar stealth) and electronic security.

RESULTS AND DISCUSSION

Synthesis and characterization of V_{n+1}C_nT_x MXenes

 V_2CT_x and $V_4C_3T_x$ (Figure 1A) were synthesized by selective removal of Al layers from the corresponding $V_{n+1}AlC_n$ MAX phase (n = 1 or 3) precursor (X-ray diffraction [XRD] patterns in Figure S1) with acid etching and subsequent delamination with tetramethylammonium hydroxide (TMAOH). Few-layer MXene flakes can be observed in scanning transmission electron microscopy (STEM) images (V_2CT_x in Figure 1B and $V_4C_3T_x$ in Figure 1E), indicating complete etching and delamination. High-angle annular dark field (HAADF) STEM images show numerous nanometer-sized defects in both V_2CT_x (Figure 1C) and $V_4C_3T_x$ (Figure 1F) flakes along the [001] zone axis, which are attributed to the chemical etching process. ¹⁹ It is noteworthy that the



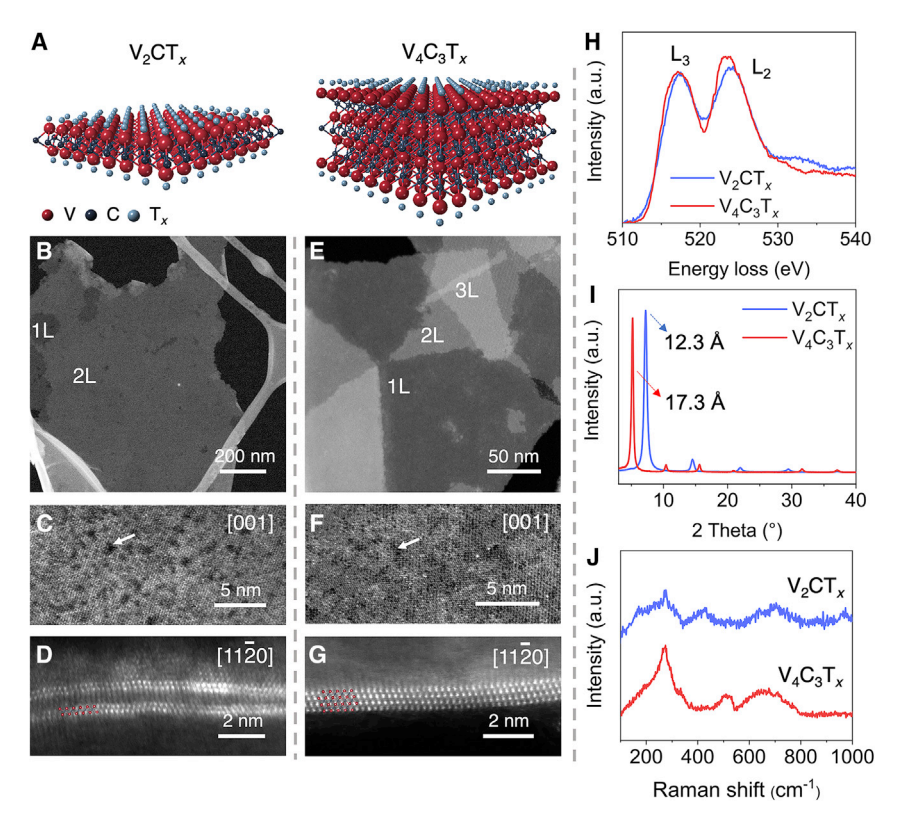


Figure 1. Characterization of V₂CT_x and V₄C₃T_x MXenes

(A) Schematic of atomic structures of V_2CT_x and $V_4C_3T_x$.

(B and E) Low-magnification TEM images of (B) V_2CT_x and (E) $V_4C_3T_x$ flakes, showing delaminated few-layer flakes.

(C and F) HAADF STEM images of (C) V_2CT_x and (F) $V_4C_3T_x$ flakes along the [001] zone axis, showing defects

(D and G) High-resolution STEM images of (D) V_2CT_x and (G) $V_4C_3T_x$ flakes along the [11 $\overline{2}$ 0] zone axis, showing layers of V_2CT_x and $V_4C_3T_x$ (bright dots are V atoms).

(H) EELS spectra of V_2CT_x and $V_4C_3T_x$ showing the different oxidation states.

(I) XRD patterns of V_2CT_x and $V_4C_3T_x$.

(G) Raman spectra of V_2CT_x and $V_4C_3T_x$.

See also Figures S1-S6.

distribution of V and C elements is not homogeneous from high-resolution energydispersive X-ray spectroscopy (EDS; Figures S2A-S2F), indicating that the defects are both micropores and vacancies in specific atomic layers. These native defects play an important role in dielectric loss, which will be discussed later. Two layers of vanadium atoms (bright spots) are observed in the cross-section of V₂CT_x (Figure 1D), while there are four vanadium layers in V₄C₃T_x (Figure 1G), confirming the crystal structure and elemental arrangement of as-synthesized $V_{n+1}C_nT_x$ MXenes. $V-L_{2,3}$ edges in electron energy-loss spectroscopy (EELS) spectra show that the $L_3/$ L_2 ratio of V_2CT_x is higher than $V_4C_3T_x$, and a weak O K edge peak appears at \sim 533 eV for V₂CT_x (Figure 1H). This indicates that V in V₂CT_x has a lower oxidation state (+3.5) than $V_4C_3T_x$ (+4), which is attributed to its fewer atomic layers, leading to all V layers bonded to surface terminations. 20 The d spacing was calculated from XRD to be 12.3 Å ($2\theta = 7.2^{\circ}$) for the V_2CT_x film and 17.3 Å ($2\theta = 5.2^{\circ}$) for the $V_4C_3T_x$ film (Figure 11). The distinct d spacings result from the different numbers of atomic layers, as illustrated in Figure 1A. The different flake thicknesses were confirmed using atomic force microscopy (Figure S3). The as-synthesized V₂CT_x and $V_4C_3T_x$ have a similar average flake size of ~ 360 nm from dynamic light



scattering (Figure S4A), avoiding the influence of flake size on the comparisons of their electronic and dielectric properties. Both have no extinction peak in the visible range and show a similar feature in UV-visible (UV-vis) spectra (Figure S4B), implying they may have similar carrier mobilities. Raman spectra show that both V_2CT_x and $V_4C_3T_x$ have broad peaks around 272 and 675 cm⁻¹ (Figure 1J), corresponding to A_{1g} symmetric and asymmetric vibrations, respectively. It is noted that E_{1g} vibration of V_2CT_x appears around 430 cm⁻¹, while it is around 510 cm⁻¹ for $V_4C_3T_x$. This is ascribed to their different chemistries. It is further confirmed by XPS spectra that V_2CT_x exhibits a higher ratio of oxygen to vanadium than $V_4C_3T_x$ (Figure S5).

EMI shielding and electronic properties

Freestanding and flexible V₂CT_x and V₄C₃T_x films were obtained by vacuum-assisted filtration from as-prepared colloidal MXene solutions (Figure S6). The V₂CT_x film had a bronze color, and the V₄C₃T_x film had a light brown color. The electrical conductivities of the films, 1,272 \pm 34 S cm⁻¹ for V₂CT_x and 1,201 \pm 39 S cm⁻¹ for V₄C₃T_x, were measured at room temperature using a four-point probe. These high conductivity values indicate that both V_2CT_x and $V_4C_3T_x$ have high EMI shielding capability. To achieve the minimum thickness of $V_{n+1}C_nT_x$ MXenes for commercial EMI shielding (EMI SE > 20 dB), we fabricated MXene coatings on glass substrates by spray coating. As shown in Figure 2A, the coatings can achieve effective EMI shielding at submicron-scale thickness (here, $V_2CT_x = 530$ nm and $V_4C_3T_x = 600$ nm). The reflection ratio of the films is >0.8 (SE_R > 6 dB), indicating the EMI shielding is mainly from reflection. Furthermore, the EMI shielding capability increases with the film thickness. The average EMI SE value of $V_4C_3T_x$ in the X band reaches 56.8 dB at a thickness of 23 μ m (Figure S7). The EMI shielding properties of freestanding V₂CT_x films of different thicknesses were reported in our previous work. We further measured the temperature (7)-dependence of resistivity (ρ) of $V_{n+1}C_nT_x$ MXenes (Figure 2B). Both V_2CT_x and $V_4C_3T_x$ have a negative $d\rho/dT$ value from 10 to 300 K, which could be attributed to the inter-flake hopping as the dominant scattering mechanism within electronic transport.²³ In contrast to V₄C₃T_{xr} V₂CT_x displays a larger decrease of resistivity with increasing temperature. This could be due to an increased relative contribution of flake-to-flake hopping in thinner MXene flakes. It is noteworthy that both V₂CT_x and V₄C₃T_x still have low resistivities even at 10 K, with a fairly flat ρ versus T for $V_4C_3T_x$ in a wide temperature range, implying that they can be used for EMI shielding at very low temperatures, e.g., at high altitude or in outer space. To better understand the intrinsic electronic properties of $V_{n+1}C_nT_x$, the dielectric function ε (ω) = ε' (ω) + $i\varepsilon''$ (ω) was studied, where the real (ε') and imaginary (ε'') parts of the dielectric constant were retrieved from the measured psi and delta by the spectroscopic ellipsometer (Figures 2C and 2D). The complex refractive index is provided in Figure S8. The error bars are derived from measurements on multiple samples with different thicknesses, showing good reproducibility. V_2CT_x and $V_4C_3T_x$ display almost identical ε' and ε'' in the visible range from 254 to 1,000 nm, suggesting the similarity in their intrinsic electronic structure. The ε' values stay positive across the scanned range for both V_2CT_x and $V_4C_3T_x$. The dielectric spectra in both V_2CT_x and $V_4C_3T_x$ were fitted with a Drude oscillator where the Kramers-Kronig relation is obeyed. The ε'' curves without optical gap indicate the metallic nature of V_2CT_x and $V_4C_3T_{xx}^{24}$ suggesting the feasibility as transparent electrodes.²⁵

Density functional theory (DFT) calculations were performed to better understand the structural and electronic properties of V_2CT_x and $V_4C_3T_x$. The atomic partial density of states (PDOS) of bare V_2C and V_4C_3 near the Fermi level suggest that both V_2C and V_4C_3 are metallic and the V-3d state is expected to provide the electrical conductivity (Figure S9). Although $V_4C_3T_x$ is predicted to be more conductive, the measured electrical conductivity values of V_2CT_x and $V_4C_3T_x$ films are similar. This



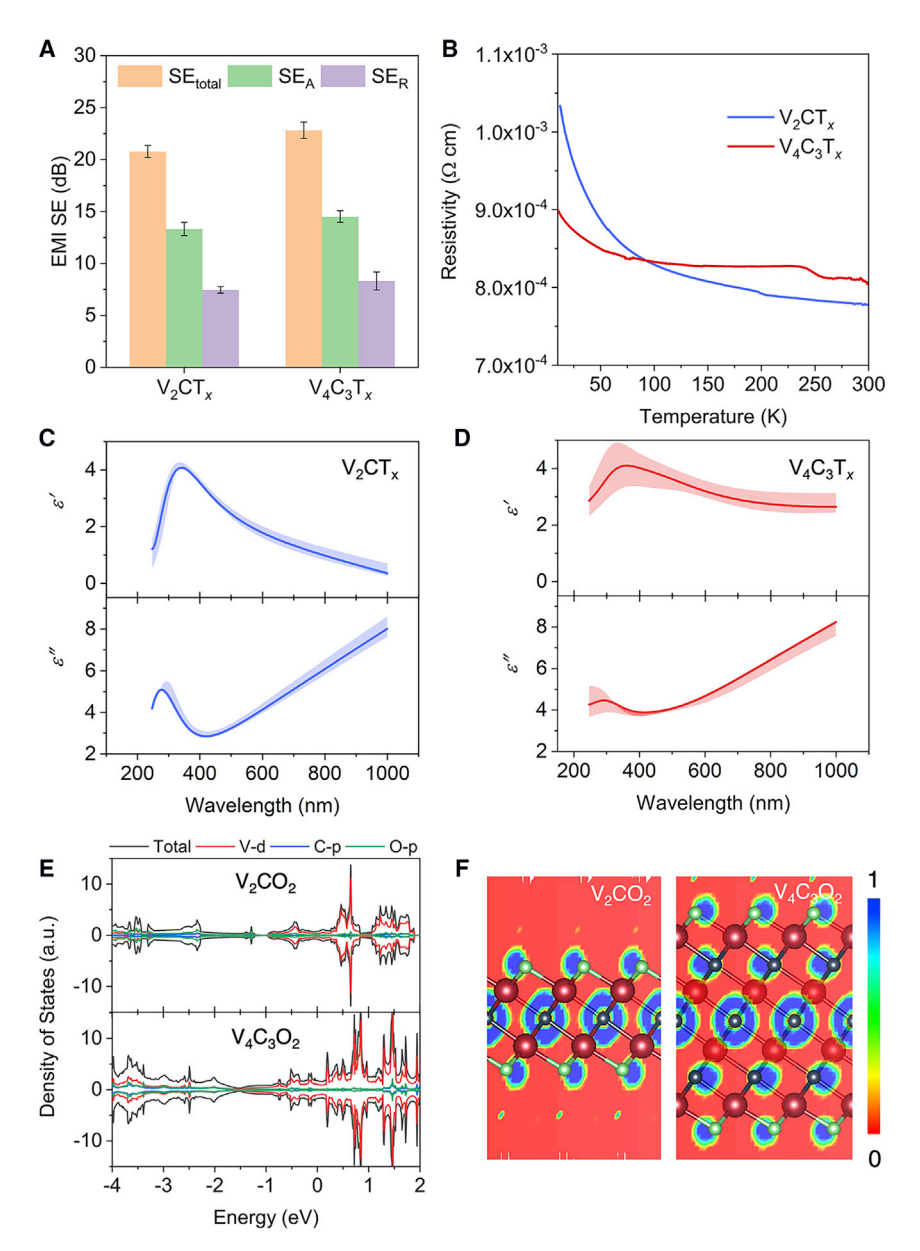


Figure 2. EMI shielding and electronic properties of $V_{n+1}C_nT_x$

(A) The average EMI shielding effectiveness (SE $_{total}$, SE $_{A}$, and SE $_{R}$) of spray-coated V $_{2}$ CT $_{x}$ (\sim 530 nm thick) and V $_{4}$ C $_{3}$ T $_{x}$ (\sim 600 nm thick) coatings on glass substrates. Data are represented as mean \pm SD.

(B) Temperature dependence of resistivity for freestanding V_2CT_x and $V_4C_3T_x$ films.

(C and D) Real (top) and imaginary (bottom) parts of dielectric constant as a function of wavelength for (C) V_2CT_x and (D) $V_4C_3T_x$ films. The shadows show variance between different film thicknesses as determined from measurements of multiple samples.

(E and F) The computed DOS (E) and electron localization function (F) of V_2CO_2 and $V_4C_3O_2$, showing the DOS change and charge distribution within layers and surface terminations, as examples.

See also Figures S7–S10.

discrepancy is likely due to native defects and different surface terminations caused by the harsher etching conditions of $V_4C_3T_x$. Upon functionalization, the atomic orbitals from the terminal groups (=O, –OH, and –F) significantly modify the PDOS. For example, in the presence of O atoms in V_2CO_2 and $V_4C_3O_2$, a strong overlapping of



O-2p and V-3d orbitals occurs in the energy range from -4 to -3 eV and attributes the bonding states between O-2p and V-3d orbitals, as illustrated in Figure 2E.

On the other hand, when the electron energy approaches the Fermi level (0 eV and above), the V-3d state prominently leads and makes the metallic bond with finite O-2p orbitals present at the Fermi level and hence makes the system conductive. The electron localization function (ELF) of bare V_2C and V_4C_3 confirms the strong metallic bonding between C and V atoms (Figures S10A and S10D). It is noteworthy that most electron density is localized near the middle C layer rather than the external two C layers in V_4C_3 . Figure 2F suggests that in the presence of O in V_2C and V_4C_3 , the majority of electron density is localized on the O atoms, ensuring charge transfer from the V atoms. The electrons are also localized around –OH and –F terminations (Figures S10B, S10C, S10E, and S10F), indicating that the surface groups influence the polarization behavior under an alternating EM field.

Microwave absorption performance

The high electrical conductivity of pristine thin V₂CT_x and V₄C₃T_x films determines their EMI shielding capability. However, it is difficult to track their absorption behavior, as strong reflection dominates. To further understand the interaction of $V_{n+1}C_nT_x$ with microwaves, we selected PU, which is microwave transparent as the matrix, and fabricated $V_{n+1}C_nT_x/PU$ composites with different MXene/PU ratios by mixing MXene colloidal solutions with water-based PU, followed by vacuum-assisted filtration to obtain films. The contents of MXene in the PU matrix were calculated based on the weight difference after annealing, as V_2CT_x and $V_4C_3T_x$ are stable under 800°C in Ar atmosphere (Figure S11). Unlike EMI shielding, which is mainly determined by the electrical conductivity, dielectric property is a key factor for microwave absorption material. For V₂CT_x/PU composites, both the real and imaginary parts of permittivity increase with the increasing content of V₂CT_x flakes. For V₂CT_x content of 1.4 wt %, the average real and imaginary parts of permittivity in the X band are 3.7 and 0.9, respectively, indicating weak dielectric loss capability. Significantly, the average values reach 5.8 (ε') and 3.1 (ε''), and the tangent loss approaches 0.5 (Figure S12), when the loading of V_2CT_x increases to 2.2 wt %. $V_4C_3T_x/PU$ composites follow a similar trend as V_2CT_x/PU composites. The average real and imaginary parts are 5.7 and 3.0 for 2.1 wt % $V_4C_3T_x$ in PU. It is noteworthy that the 2.8 wt % V_2CT_x/PU composite shows a higher permittivity than the 3.2 wt % V₄C₃T_x/PU composite. Since V_2CT_x has fewer atomic layers than $V_4C_3T_x$, there are more V_2CT_x flakes in the composite at the same MXene mass in the composite. This abundance of flakes can more easily facilitate the formation of a localized percolatively conductive network.

To evaluate the microwave absorption capability of as-fabricated composites, reflection loss (RL) was calculated based on the measured permittivity (Equations 4 and 5). When the filler ratios are low (1.4 wt %, V_2CT_x and 1.0 wt %, $V_4C_3T_x$), both V_2CT_x /PU and $V_4C_3T_x$ /PU do not provide effective EM wave absorption (RL < -10 dB) at any thicknesses up to 4 mm due to the weak dielectric loss of <0.3 (Figures S13A and S13D). In contrast, when the filler ratios are too high (2.8 wt %, V_2CT_x and 3.2 wt %, $V_4C_3T_x$), their EM wave absorption performance is poor as well. It is attributed to the impedance mismatch with free space caused by the excessive dielectric loss of >1.0 (Figure S12). For composites with 2.2 wt % V_2CT_x (d=3.3 mm) and 2.1 wt % $V_4C_3T_x$ (d=3.4 mm), the effective absorption covers the whole X band, and the minimum RL values reach -30 and -39 dB, respectively (Figures 3C, S13B, and S13E). This optimal absorption performance was achieved with a "moderate" permittivity (ε ', \sim 6 and ε ", \sim 3) and tangent loss (\sim 0.5). The EM



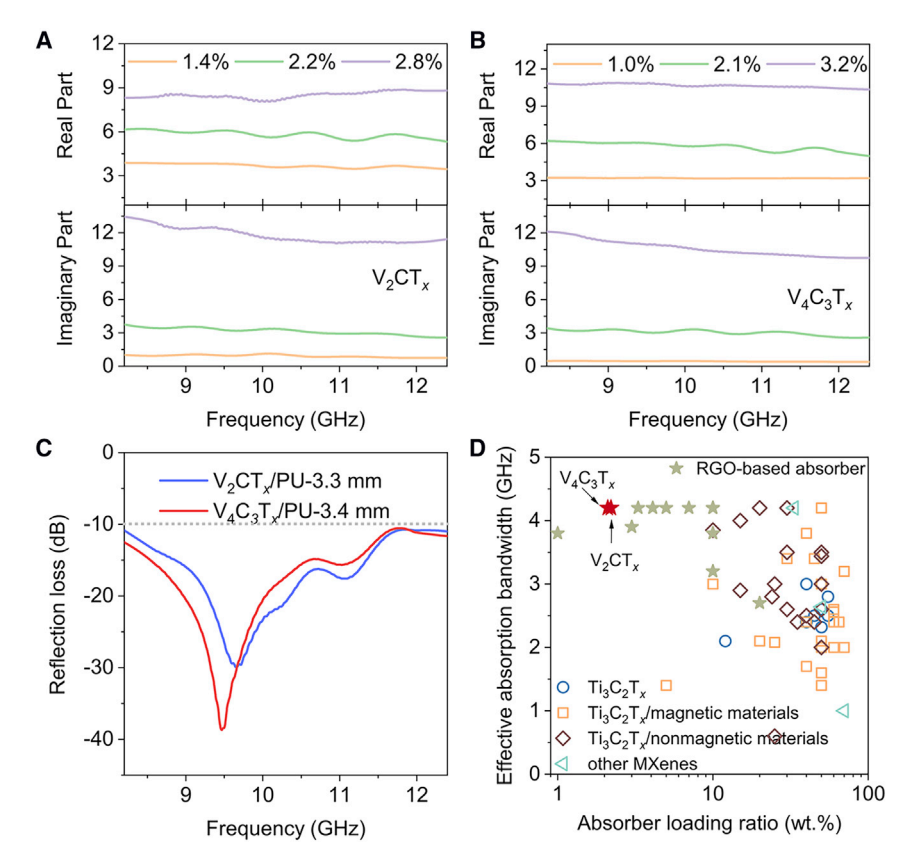


Figure 3. Dielectric and microwave absorption properties of $V_{n+1}C_nT_x/polyurethane$ composites (A and B) Permittivity of (A) V_2CT_x/PU and (B) $V_4C_3T_x/PU$ composites with different MXene contents in the X band.

(C) Calculated reflection loss of V_2CT_x/PU (2.2 wt %) and $V_4C_3T_x/PU$ composites (2.1 wt %) at optimized thicknesses, showing that $V_{n+1}C_nT_x/PU$ composites with ultralow loading ratios achieve effective absorption in the whole X band.

(D) Comparison of EM wave absorption performance of $V_{n+1}C_nT_x/PU$ composites with reported $Ti_3C_2T_{x}$ -based composites, RGO-based composites, and other materials. Effective absorption bandwidth versus filler ratio of absorber in the matrix. $V_{n+1}C_nT_x/PU$ composites outperform all $Ti_3C_2T_{x}$ - and other MXene-based composites, as well as RGO-based composites. See also Figures S12 and S13 and Tables S1 and S2.

wave absorption performance of $V_{n+1}C_nT_x/PU$ composites was compared with Ti₃C₂T_x-based composites, reduced graphene oxide (RGO)-based composites, and other MXene-based composites in Figure 3D (details are provided in Tables S1 and S2). Compared with this work, pure Ti₃C₂T_x-based absorption materials (Figure 3D, blue circles) have high filler loadings (>10 wt %) and narrow (<3 GHz) absorption bandwidth in the X band. In past years, most studies enlarged the effective absorption frequency range with additional absorption-enhancing additives, including magnetic metals (Fe, Co, Ni, FeCo, etc.), magnetic oxides (Fe₂O₃, Fe₃O₄, and ferrites), carbon materials (nanotubes, carbon fiber, graphite, etc.), semiconductors (SiC, MoS₂, TiO₂, etc.), and others. However, multiple additives complicate fabrication and usually increase the weight, limiting practical applications. In contrast, V₂CT_x- and V₄C₃T_x-based composites with ultralow loadings (~2 wt %) have a simple fabrication process and achieve effective absorption in the entire X band. This performance compares well with widely studied RGO-based composites, which have been regarded as the most promising materials to replace ferrites for microwave absorption in the past decade.²⁶ Further performance gain can be



expected from improved dispersion of vanadium MXenes in the polymer matrix, as well as from exploration of a very large number of other MXenes available. 16,17

To understand the absorption mechanisms of $V_{n+1}C_nT_x/PU$ composites, MXene dispersion within the matrix was studied using high-resolution TEM (HRTEM; Figures 4A, 4B, and S14). MXene layers are intercalated and confined in PU, which is further confirmed by the shift and broadening of (002) peaks from the XRD patterns of $V_{n+1}C_nT_x/PU$ composites (Figure S15). More importantly, due to the vacuum-assisted filtration process, MXene flakes in the PU matrix tend to align parallel to the film surface, which makes the incident EM waves' propagation direction to be normal to the planar flakes. The flake arrangement coupled with the 2D nature of MXene builds a localized percolatively conductive network with electron transport channels. The connected MXene flakes facilitate the paths for electron hopping, which can contribute to EM wave dissipation with conductor loss. Additionally, since these aligned flakes are intercalated with a dielectric layer of PU, they can be treated as numerous microcapacitors, which leads to the charge accumulation in an alternating EM field. Semiconductors, such as SiC or ZnO, are typically preferred as absorption phases for non-magnetic absorption materials due to their moderate conductivity and permittivity.^{27,28} However, metallic V₂CT_x and V₄C₃T_x benefit from the electron transport, which directly correlates to conduction loss for incident EM waves. Moreover, the defects and random surface terminations in MXene flakes give rise to the charge asymmetric distribution (Figures 4C and 4D). Meanwhile, the heterointerfaces between MXene and PU can also accumulate electrons under EM field. These redistributed charges generate dipoles, which lead to relaxation behaviors in the EM field and eventually enhance EM wave attenuation.^{29,30} Given that the dielectric properties of pristine $V_{n+1}C_nT_x$ are in the required range for microwave absorption, it is expected that its absorption performance can be further improved by surface modification. Our calculations show that surface terminations have a significant impact on the electronic structure of $V_{n+1}C_nT_x^{-21}$ From this perspective, the control of defects and surface groups in MXenes can be an effective route to adjust their dielectric properties and further optimize the absorption capability. On the other hand, we have previously demonstrated that the electronic properties of MXenes can be controlled with a large number of compositions through M-site solid solutions.³¹ This could be another approach to tailoring permittivity and dielectric loss. Moreover, the predictions have shown that some MXenes can be magnetic, 32-34 which provides an opportunity to design MXene-based absorbers with additional magnetic loss.

In summary, we have demonstrated that vanadium-based MXenes (V_2CT_x and $V_4C_3T_x$) can be used as EMI shielding coatings with a submicrometer thickness. What is even more important, both V_2CT_x and $V_4C_3T_x$ exhibit efficient EM wave absorption in the whole X band when incorporated into a PU matrix with ultralow mass loadings (\sim 2 wt%). V_2CT_x and $V_4C_3T_x$ have sufficient dielectric losses and lower electrical conductivity than $Ti_3C_2T_x$, enabling an advantageous balance between impedance match and EM wave attenuation. The surface terminations of MXenes influence the polarization behavior under an alternating EM field. The free carriers, native defects, and surface groups in MXene flakes associated with the well-aligned layers in the composites establish vanadium-based MXenes as a promising platform for rational design of EM wave absorbers.

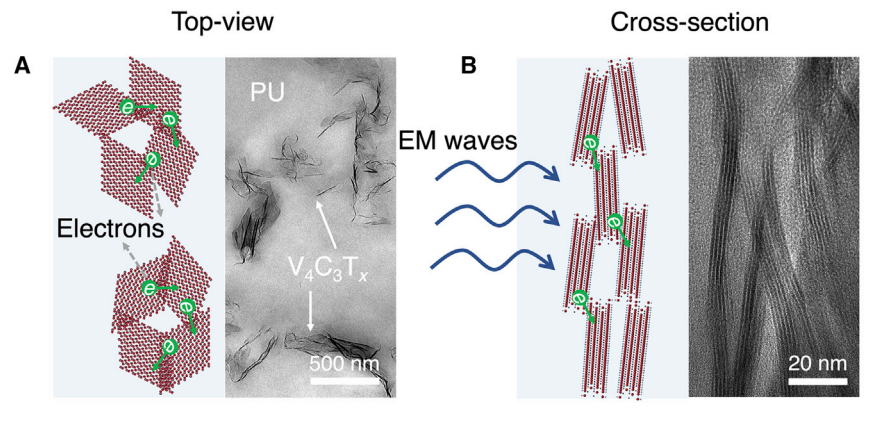
EXPERIMENTAL PROCEDURES

Resource availability

Lead contact

Further information and requests for resources and reagents should be directed to and will be fulfilled by the lead contact, Yury Gogotsi@drexel.edu).





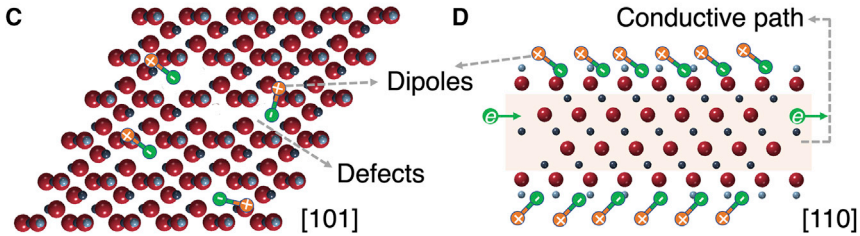


Figure 4. Microwave absorption mechanism of $V_{n+1}C_nT_x/polyurethane$ composites (A and B) Schematics and TEM images of vacuum-filtered $V_4C_3T_x/PU$ composite: (A) top view and (B) cross-section. Here, the $V_4C_3T_x/PU$ composite is used as an example. (C and D) Atomic structure schematics of $V_4C_3T_x$: (C) (101) plane shows vacancies contributing to defect polarization, and (D) (110) plane shows metallic conductive behavior and dipole

defect polarization, and (D) (110) plane shows metallic conductive behavior and dipole polarization, which is attributed to surface terminations.

See also Figure S14.

Materials availability

This study did not generate new unique reagents.

Data and code availability

The data supporting the current study are available from the corresponding author upon reasonable request.

Preparation of materials

The following materials were used: V (99.5%, -325 mesh, Alfa Aesar), Al (99.5%, -325 mesh, Alfa Aesar), C (graphite, 99%, -325 mesh, Alfa Aesar), hydrofluoric acid (HF; 48.5–51%, Acros Organics), HCl (36.5–38%, Fisher Chemical), TMAOH (25 wt %, Acros Organics), and water-based PU dispersion (32.5–36.5 wt %, Dainichiseika Color & Chemicals).

Synthesis of V_{n+1}AlC_n MAX phases

For V_2AlC , the precursor V:Al:C powders were mixed in an atomic ratio of 2:1.1:0.9, following previous reports. ⁴ The powders were ball milled at 70 RPM for 18 h with zirconia balls (2:1 mass ratio of balls to powder). The mixed powder was then placed into an alumina crucible, which was placed into a high-temperature furnace and heated at 1,550°C for 2 h with Ar continually flowing at 200 sccm. The heating and cooling rates are 3°C min⁻¹. The sintered compact was milled and sieved to below 32 μ m. The powder was washed with 9 M HCl for 24 h to remove residual intermetallics and metals, then was repeatedly washed with deionized (DI)



water. For V_4AIC_3 , a similar procedure was followed, except the precursors V:Al:C were mixed in a 4:1.5:3 atomic ratio, and the mixed powder was sintered at $1,500^{\circ}C$ for 2 h.

Synthesis of $V_{n+1}C_nT_x$ MXenes

 V_2CT_x and $V_4C_3T_x$ were synthesized by the selective etching of the corresponding MAX phases (V_2AIC and V_4AIC_3) with HF. Typically, 1 g V_2AIC powder was added slowly into 20 mL HF. The mixture was stirred at 35°C for 48 h. After etching, the reacted solution was repeatedly washed with DI water through centrifugation at 3,500 RPM for 2 min until pH >6. For delamination, 1 g TMAOH was added into the washed sediment with 10 mL DI water and then stirred for 24 h. After stirring, the mixture was centrifuged repeatedly with DI water at 10,000 RPM for 10 min until pH <8. At last, the solution was centrifuged at 3,500 RPM for 10 min to collect supernatant. For V_4AIC_3 , a similar procedure was followed, except the etching time was 8 days and the delamination time was 48 h.

Fabrication of MXene films

Freestanding MXene films were fabricated through vacuum-assisted filtration with a Celgard 3501 membrane. MXene films on glass substrate were obtained by spray-coating method. Before spray coating, the glass slide (Thermo Fisher Scientific) was sonicated in ethanol and then plasma treated (Tergeo Plus, Pie Scientific) at 100 W for 5 min with oxygen flow at 3 sccm. All MXene films were dried in a vacuum oven at 80°C for 12 h.

Fabrication of MXene/PU composites

MXene/PU composites were fabricated using the vacuum-assisted filtration method. Before the fabrication, the concentration of MXene solution was calculated through the filtered MXene film. Typically, a certain amount of MXene colloidal solution (V_2CT_x or $V_4C_3T_x$) was mixed with water-based PU dispersion and stirred for 1 h at room temperature. The mixture was vacuum filtered to obtain MXene/PU gel. The gel was dried in vacuum at room temperature for 24 h. At last, the composite was obtained after drying in vacuum at 80°C for 12 h. The weight ratio of MXene in the composite was calculated based on thermogravimetric analysis (TGA).

Characterization

HAADF STEM images were obtained with a JEOL NEOARM operating at 200 kV. For imaging, the camera length was 4 cm with a probe current of 150 pA. EELS maps were obtained with a camera length of 2 cm and a probe current of 150 pA. A K2 Summit camera, provided by Gatan, was used for recording EELS spectra. Brightfield TEM images of $V_{n+1}C_nT_x/PU$ were obtained with a JEOL F200 operating at 200 kV. The $V_{n+1}C_nT_x/PU$ cross-sections were fabricated by embedding the samples in epoxy resin and then cutting them with a microtome. XRD patterns of MAX phases and MXene films were measured using a Rigaku SmartLab (Tokyo, Japan) operating at 40 kV/30 mA with Cu K α radiation. Raman measurement was carried out with an inverted reflection mode Renishaw (2008, Gloucestershire, UK) instrument, equipped with a $63 \times$ (numerical aperture [NA] = 0.7) objective and a diffraction-based room temperature spectrometer. The laser line used was 633 nm, and the laser power was kept around 0.1 mW. A 3D laser scanning confocal microscope (Keyence, VK-X1000, Osaka, Japan) was used to observe MXene coating and measure the thickness. The electrical conductivity of MXene films was measured using the fourpoint probe instrument (ResTest, Jandel Engineering, Bedfordshire, UK), with a probe distance of 1 mm. An average value was taken from 3 different locations on

Article



the film. A Quantum Design EverCool II Physical Property Measurement System (PPMS) was used to measure the dependence of resistivity on temperature (10–300 K) in a low pressure of helium (<5 Torr). MXene films were wired into a four-point probe geometry with silver paint. UV-vis spectroscopy was performed on MXene-coated glass slides from 250 to 1,000 nm (Evolution 201, Thermo Fisher Scientific). Wavelength-dependent optical absorption and the permittivity was measured by a J.A. Woollam M-200U variable-angle spectroscopic ellipsometer. The data were collected at 65°, 67.5°, 70°, 72.5°, and 75°. Different batches of V_2CT_x and $V_4C_3T_x$ samples (spray coated on Si/SiO₂ substrates) with varied thicknesses were measured at three different spots, confirming the reproducibility of the spectra. The general oscillator model was used to fit the experimental spectra using Woollam WVASE software.

A vector network analyzer (VNA; 8720ES, Agilent, Santa Clara, CA, USA) with a WR-90 rectangular waveguide in the frequency range of 8.2–12.4 GHz was used to measure *S* parameters of MXene films and the permittivity of MXene/PU composites. For the waveguide calibration, a standard calibration kit (X11644A, WR-90, Keysight) was used to complete the calibration manually. The calibration procedure included "through," "short plate," and "transmission line" tests in turn. After calibration, a pure Teflon sample with a known permittivity was tested to make sure that the calibration is correct.

For EMI shielding performance, the EMI SE was calculated based on S parameters $(S_{11} \text{ and } S_{21})$. The transmission power $(T; T = |S_{21}|^2)$, reflectivity power $(R; R = |S_{11}|^2)$, and absorption power (A) meet A + R + T = 1. The total EMI SE (SE_{total}) , reflection effectiveness (SE_R) , and absorption effectiveness (SE_A) associated with the incident wave P_1 and transmitted wave P_T are calculated as follows:

$$SE_{total} = 10log_{10}\left(\frac{1}{T}\right),$$
 (Equation 1)

$$SE_R = 10log_{10}\left(\frac{1}{1-R}\right),$$
 (Equation 2)

and

$$SE_A = 10log_{10} \left(\frac{1 - R}{T} \right).$$
 (Equation 3)

For microwave absorption performance, the RL was calculated using the measured permittivity at a given layer thickness and frequency by the following equations:³⁵

$$RL(dB) = 20log_{10}|(Z_{in} - 1) / (Z_{in} + 1)|$$
 (Equation 4)

and

$$Z_{\rm in} = \sqrt{\frac{\mu}{\varepsilon}} \tanh(j2\pi\sqrt{\mu\varepsilon} \, \text{fd} / c),$$
 (Equation 5)

where Z_{in} is the normalized input impedance of the microwave absorption layer, ε and μ are the relative permittivity and permeability of the samples, respectively, f is the microwave frequency, d is the absorption layer thickness, and c is the light velocity in vacuum. As V_2CT_x and $V_4C_3T_x$ are non-magnetic, the real and imaginary parts of their permeability are 1 and 0, respectively. Effective absorption is achieved when the RL value is below -10 dB, indicating more than 90% of microwave is absorbed. The corresponding frequency range is defined as the effective absorption bandwidth.



DFT calculations

All the calculations were performed using DFT as implemented with the standard frozen-core projector augmented-wave (PAW) method in the Vienna ab initio simulation package (VASP). 36,37 The electronic exchange and correlation are approximated by the Perdew-Burke-Ernzerhof (PBE) form of the generalized gradient approximation (GGA). $^{38-40}$ Kinetic energy cutoff of the plane wave expansion is set to 520 eV. All the structures are entirely relaxed until the component of the Hellmann-Feynman forces is less than 0.005 eV/Å. A Monkhorst-Pack k-point mesh of 21 × 21 × 1 is used for the relaxation. 41 To avoid any spurious cell-cell interaction among the periodic images of the 2D sheets, a large vacuum space of 20 Å is introduced in the z direction. The DOS and ELF calculations are done using a denser 21 × 21 × 1 k-grid.

The optimized lattice constant of V_2C and V_4C_3 is 2.90 and 2.92 Å, respectively. The layer thickness d, defined as the V-V distance, is equal to 2.17 (V_2C) and 2.26 Å (V_4C_3). We have constructed functionalized V_2CT_2 and $V_4C_3T_2$ MXene structures with T=O, F, and F0H terminations based on their pristine unit-cell F1C and F2C and F3. To find the ground-state geometry of F3C and F4C and F4C and F4C and F5C and F7C and F8C and F9C and

SUPPLEMENTAL INFORMATION

Supplemental information can be found online at https://doi.org/10.1016/j.xcrp. 2022.101073.

ACKNOWLEDGMENTS

This work was supported by the US National Science Foundation (grant ECCS-2034114) and Murata Manufacturing Co., Ltd. (Japan). Ellipsometry and temperature-dependent resistivity measurements (Y.Y. and S.J.M.) were supported by US Department of Energy (DOE), Office of Science, Office of Basic Energy Sciences, grant DE-SC0018618. We thank Mark Anayee, Dr. Dipna A. Patel, Dr. Kanit Hantanasirisakul, Teng Zhang, and Geetha Valurouthu for assistance in MXene characterization.

AUTHOR CONTRIBUTIONS

Conceptualization, M.H. and Y.G.; methodology, M.H., C.E.S., A.S., Y.Y., A.C.F., and A.G.; investigation, M.H., C.E.S., A.S., Y.Y., A.C.F., A.G., and B.M.; funding acquisition, S.J.M. and Y.G.; project administration, Y.G.; supervision, S.J.M., V.B.S., E.A.S., and Y.G.; writing – original draft, M.H., A.S., Y.Y., and A.C.F.; writing – review & editing, C.E.S., A.G., B.M., S.J.M., V.B.S., E.A.S., and Y.G.

DECLARATION OF INTERESTS

The authors declare no competing financial interests.

Received: July 10, 2022 Revised: August 29, 2022 Accepted: September 9, 2022 Published: September 27, 2022

Article



REFERENCES

- VahidMohammadi, A., Rosen, J., and Gogotsi, Y. (2021). The world of two-dimensional carbides and nitrides (MXenes). Science 372, eabf1581. https://doi.org/10.1126/science. abf1581.
- Wei, Q., Pei, S., Qian, X., Liu, H., Liu, Z., Zhang, W., Zhou, T., Zhang, Z., Zhang, X., and Cheng, H.M. (2020). Superhigh electromagnetic interference shielding of ultrathin aligned pristine graphene nanosheets film. Adv. Mater. 32, 1907411. https://doi.org/10.1002/adma. 201907411.
- Balci, O., Polat, E.O., Kakenov, N., and Kocabas, C. (2015). Graphene-enabled electrically switchable radar-absorbing surfaces. Nat. Commun. 6, 6628. https://doi. org/10.1038/ncomms7628.
- Han, M., Shuck, C.E., Rakhmanov, R., Parchment, D., Anasori, B., Koo, C.M., Friedman, G., and Gogotsi, Y. (2020). Beyond Ti₃C₂T_x: MXenes for electromagnetic interference shielding. ACS Nano 14, 5008– 5016. https://doi.org/10.1021/acsnano. 0c01312.
- Shahzad, F., Alhabeb, M., Hatter, C.B., Anasori, B., Hong, S.M., Koo, C.M., and Gogotsi, Y. (2016). Electromagnetic interference shielding with 2D transition metal carbides (MXenes). Science 353, 1137–1140. https://doi.org/10. 1126/science.aag2421.
- Yun, T., Kim, H., Iqbal, A., Cho, Y.S., Lee, G.S., Kim, M.K., et al. (2020). Electromagnetic shielding of monolayer MXene assemblies. Adv. Mater. 32, 1906769. https://doi.org/10. 1002/adma.201906769.
- Lipton, J., Röhr, J.A., Dang, V., Goad, A., Maleski, K., Lavini, F., Han, M., Tsai, E.H.R., Weng, G.-M., Kong, J., et al. (2020). Scalable, highly conductive, and micropatternable MXene films for enhanced electromagnetic interference shielding. Matter 3, 546–557. https://doi.org/10.1016/j.matt.2020.05.023.
- 8. Wan, S., Li, X., Chen, Y., Liu, N., Du, Y., Dou, S., Jiang, L., and Cheng, Q. (2021). High-strength scalable MXene films through bridging-induced densification. Science 374, 96–99. https://doi.org/10.1126/science.abg2026.
- Iqbal, A., Shahzad, F., Hantanasirisakul, K., Kim, M.-K., Kwon, J., Hong, J., Kim, H., Kim, D., Gogotsi, Y., and Koo, C.M. (2020). Anomalous absorption of electromagnetic waves by 2D transition metal carbonitride Ti₃CNT_x (MXene). Science 369, 446–450. https://doi.org/10.1126/ science.aba7977.
- Yin, X., Kong, L., Zhang, L., Cheng, L., Travitzky, N., and Greil, P. (2014). Electromagnetic properties of Si-C-N based ceramics and composites. Int. Mater. Rev. 59, 326–355. https://doi.org/10.1179/1743280414Y. 0000000037.
- Mirkhani, S.A., Shayesteh Zeraati, A., Aliabadian, E., Naguib, M., and Sundararaj, U. (2019). High dielectric constant and low dielectric loss via poly(vinyl alcohol)/Ti₃C₂T_x MXene nanocomposites. ACS Appl. Mater. Interfaces 11, 18599–18608. https://doi.org/10. 1021/acsami.9b00393.

- Han, M., Yin, X., Wu, H., Hou, Z., Song, C., Li, X., Zhang, L., and Cheng, L. (2016). Ti₃C₂ MXenes with modified surface for high-performance electromagnetic absorption and shielding in the X-band. ACS Appl. Mater. Interfaces 8, 21011–21019. https://doi.org/10.1021/acsami. 6b06455.
- Cao, M.-S., Cai, Y.-Z., He, P., Shu, J.-C., Cao, W.-Q., and Yuan, J. (2019). 2D MXenes: electromagnetic property for microwave absorption and electromagnetic interference shielding. Chem. Eng. J. 359, 1265–1302. https://doi.org/10.1016/j.cej.2018.11.051.
- Zhang, Z., Cai, Z., Zhang, Y., Peng, Y., Wang, Z., Xia, L., Ma, S., Yin, Z., Wang, R., and Cao, Y. (2021). The recent progress of MXene-based microwave absorption materials. Carbon 174, 484–499. https://doi.org/10.1016/j.carbon. 2020.12.060.
- Shekhirev, M., Shuck, C.E., Sarycheva, A., and Gogotsi, Y. (2021). Characterization of MXenes at every step, from their precursors to single flakes and assembled films. Prog. Mater. Sci. 120, 100757. https://doi.org/10.1016/j.pmatsci. 2020 100757.
- Naguib, M., Barsoum, M.W., and Gogotsi, Y. (2021). Ten years of progress in the synthesis and development of MXenes. Adv. Mater. 33, 2103393. https://doi.org/10.1002/adma. 202103393.
- Deysher, G., Shuck, C.E., Hantanasirisakul, K., Frey, N.C., Foucher, A.C., Maleski, K., Sarycheva, A., Shenoy, V.B., Stach, E.A., Anasori, B., and Gogotsi, Y. (2020). Synthesis of Mo₄VAIC₄ MAX phase and twodimensional Mo₄VC₄ MXene with five atomic layers of transition metals. ACS Nano 14, 204–217. https://doi.org/10.1021/acsnano. 9b07708.
- Tran, M.H., Schäfer, T., Shahraei, A., Dürrschnabel, M., Molina-Luna, L., Kramm, U.I., and Birkel, C.S. (2018). Adding a new member to the MXene family: synthesis, structure, and electrocatalytic activity for the hydrogen evolution reaction of V₄C₃T_x. ACS Appl. Energy Mater. 1, 3908–3914. https://doi.org/10.1021/ acsaem.8b00652.
- Sang, X., Xie, Y., Lin, M.-W., Alhabeb, M., Van Aken, K.L., Gogotsi, Y., Kent, P.R., Xiao, K., and Unocic, R.R. (2016). Atomic defects in monolayer titanium carbide (Ti₃C₂T_x) MXene. ACS Nano 10, 9193–9200. https://doi.org/10. 1021/acsnano.6b05240.
- Foucher, A.C., Han, M., Shuck, C.E., Maleski, K., Gogotsi, Y., and Stach, E.A. (2022). Shifts in valence states in bimetallic MXenes revealed by electron energy-loss spectroscopy (EELS).
 D Mater. 9, 025004. https://doi.org/10.1088/ 2053-1583/ac4ba2.
- Maleski, K., Shuck, C.E., Fafarman, A.T., and Gogotsi, Y. (2020). The broad chromatic range of two-dimensional transition metal carbides. Adv. Opt. Mater. 9, 2001563. https://doi.org/ 10.1002/adom.202001563.
- Champagne, A., Shi, L., Ouisse, T., Hackens, B., and Charlier, J.-C. (2018). Electronic and vibrational properties of V₂C-based MXenes: from experiments to first-principles modeling.

- Phys. Rev. B 97, 115439. https://doi.org/10.1103/PhysRevB.97.115439.
- Hart, J.L., Hantanasirisakul, K., Lang, A.C., Anasori, B., Pinto, D., Pivak, Y., van Omme, J.T., May, S.J., Gogotsi, Y., and Taheri, M.L. (2019). Control of MXenes' electronic properties through termination and intercalation. Nat. Commun. 10, 1–10. https://doi.org/10.1038/ s41467-018-08169-8.
- Dillon, A.D., Ghidiu, M.J., Krick, A.L., Griggs, J., May, S.J., Gogotsi, Y., Barsoum, M.W., and Fafarman, A.T. (2016). Highly conductive optical quality solution-processed films of 2D titanium carbide. Adv. Funct. Mater. 26, 4162– 4168. https://doi.org/10.1002/adfm. 201600357.
- Jiang, X., Kuklin, A.V., Baev, A., Ge, Y., Ågren, H., Zhang, H., and Prasad, P.N. (2020). Twodimensional MXenes: from morphological to optical, electric, and magnetic properties and applications. Phys. Rep. 848, 1–58. https://doi. org/10.1016/j.physrep.2019.12.006.
- 26. Song, Q., Ye, F., Kong, L., Shen, Q., Han, L., Feng, L., Yu, G., Pan, Y., and Li, H. (2020). Graphene and MXene nanomaterials: toward high-performance electromagnetic wave absorption in gigahertz band range. Adv. Funct. Mater. 30, 2000475. https://doi.org/10.1002/adfm.202000475.
- Lan, X., and Wang, Z. (2020). Efficient hightemperature electromagnetic wave absorption enabled by structuring binary porous SiC with multiple interfaces. Carbon 170, 517–526. https://doi.org/10.1016/j.carbon.2020.08.052.
- Han, M., Yin, X., Kong, L., Li, M., Duan, W., Zhang, L., et al. (2014). Graphene-wrapped ZnO hollow spheres with enhanced electromagnetic wave absorption properties. J. Mater. Chem. A 2, 16403–16409. https://doi. org/10.1039/C4TA03033H.
- Wen, B., Cao, M., Lu, M., Cao, W., Shi, H., Liu, J., Wang, X., Jin, H., Fang, X., Wang, W., and Yuan, J. (2014). Reduced graphene oxides: light-weight and high-efficiency electromagnetic interference shielding at elevated temperatures. Adv. Mater. 26, 3484– 3489. https://doi.org/10.1002/adma. 201400108.
- Wang, X.-X., Zhang, M., Shu, J.-C., Wen, B., Cao, W.-Q., and Cao, M.-S. (2021). Thermallytailoring dielectric "genes" in graphene-based heterostructure to manipulate electromagnetic response. Carbon 184, 136–145. https://doi. org/10.1016/j.carbon.2021.07.099.
- Han, M., Maleski, K., Shuck, C.E., Yang, Y., Glazar, J.T., Foucher, A.C., Hantanasirisakul, K., Sarycheva, A., Frey, N.C., May, S.J., et al. (2020). Tailoring electronic and optical properties of MXenes through forming solid solutions. J. Am. Chem. Soc. 142, 19110–19118. https:// doi.org/10.1021/jacs.0c07395.
- Frey, N.C., Bandyopadhyay, A., Kumar, H., Anasori, B., Gogotsi, Y., and Shenoy, V.B. (2019). Surface-engineered MXenes: electric field control of magnetism and enhanced magnetic anisotropy. ACS Nano 13, 2831– 2839. https://doi.org/10.1021/acsnano. 8509201



Cell Reports Physical Science Article

- Zhang, Y., Cui, Z., Sa, B., Miao, N., Zhou, J., and Sun, Z. (2022). Computational design of double transition metal MXenes with intrinsic magnetic properties. Nanoscale Horiz. 7, 276–287. https://doi.org/10.1039/D1NH00621E.
- Kim, H., and Alshareef, H.N. (2020). MXetronics: MXene-enabled electronic and photonic devices. ACS Mater. Lett. 2, 55–70. https://doi.org/10.1021/acsmaterialslett. 9b00419.
- 35. Miles, P., Westphal, W., and Von Hippel, A. (1957). Dielectric spectroscopy of ferromagnetic semiconductors. Rev. Mod. Phys. 29, 279. https://doi.org/10.1103/RevModPhys.29.279.
- 36. Kresse, G., and Furthmüller, J. (1996). Efficiency of ab-initio total energy calculations for metals and semiconductors using a plane-wave basis set. Comput. Mater. Sci. 6, 15–50. https://doi.org/10.1016/0927-0256(96)00008-0.
- Fuchs, M., and Scheffler, M. (1999). Ab initio pseudopotentials for electronic structure calculations of poly-atomic systems using density-functional theory. Comput. Phys. Commun. 119, 67–98. https://doi.org/10.1016/ S0010-4655(98)00201-X.
- 38. Kresse, G., and Furthmüller, J. (1996). Efficient iterative schemes for ab initio total-energy calculations using a plane-wave basis set. Phys.

- Rev. B 54, 11169. https://doi.org/10.1103/ PhysRevB.54.11169.
- Perdew, J.P., Burke, K., and Ernzerhof, M. (1996). Generalized gradient approximation made simple. Phys. Rev. Lett. 77, 3865. https:// doi.org/10.1103/PhysRevLett.77.3865.
- 40. Perdew, J., Burke, K., and Ernzerhof, M. (1998). Perdew, Burke, and Ernzerhof reply. Phys. Rev. Lett. 80, 891. https://doi.org/10.1103/ PhysRevLett.80.891.
- 41. Monkhorst, H.J., and Pack, J.D. (1976). Special points for Brillouin-zone integrations. Phys. Rev. B 13, 5188. https://doi.org/10.1103/PhysRevB.13.5188.